1

Development of Thermoelectric materials based on $NaTaO_3$ - composite ceramics

Wilfried Wunderlich[1] and Bernd Baufeld[2]
[1] *Tokai University, Dept. Material Science., Kitakaname 1117, Hiratsuka-shi, Japan*
[2] *Kath. Universiteit Leuven, Dpt MTM Metallurgy and Ma. Eng., Leuven, Belgium*

1. Introduction

This chapter describes the development of novel thermoelectric materials for high-temperature applications like gas burners, combustion engines, nuclear fuel, or furnaces. The goal of this development is to recycle waste heat for energy harvesting in order to contribute in saving the environment. The research results are described in the following sub-chapters in four different sections.

After a general review about perovskites and $NaTaO_3$ in section 2, *ab-initio*-simulations of the Seebeck coefficient are described in section 3. The Seebeck coefficient strongly depends on the effective mass and carrier concentration. The electronic band-structure calculations showed a large electron effective mass for $NaTaO_3$. Heavily doping changes $NaTaO_3$'s band-structure in a similar way as the well-known thermoelectric material Nb-doped $SrTiO_3$. Hence, $NaTaO_3$, which is stable up 2083 K and which is known as a material with excellent photo-catalytic properties, was chosen as a candidate for thermoelectric materials.

Section 4 describes the finding of suitable doping elements by sintering $NaTaO_3$ with different raw materials. While both, pure $NaTaO_3$ and $NaTaO_3$ sintered with Fe_2O_3, are almost insulators, it was discovered that sintering with metallic iron increases both, electric conductivity and Seebeck coefficient. Microstructural characterization by SEM and XRD measurements showed that a $NaTaO_3$-Fe_2O_3 composite material is formed. The amount of Fe solved in the $NaTaO_3$ lattice is much higher when the starting materials consist of Fe instead of Fe_2O_3. Addition of several metals like Mn, Cr, Ti, Ni, Cu, Mo, W, Fe, and Ag were tested, but only the later two elements lead to remarkable electric conductivity observed above 773 K.

Section 5 describes the measurement of thermoelectric properties such as Seebeck-voltage at a large temperature gradient, a method which is close to applications, but not yet commonly used, because the thermoelectric theory is based on small temperature gradients. Thermal conductivity is not measured, but only estimated. The doping is achieved by sintering metallic iron or silver together with $NaTaO_3$. The results are high negative Seebeck voltages up to -320 mV at a temperature difference of 700 K, as well as high closed-circuit currents up to -250 μA for Fe-doping and positive values for Ag-doping. Besides reporting previous results, several new findings are described here for the first time. Composites with Cu yield

to a small Seebeck voltage of about -10 mV with a strong response, when heat flow direction is reversed.
In section 6 the thermokinetic measurement by differential scanning calorimetry (DSC) and thermoanalysis (TA) clarifies the reaction sintering between Fe and $NaTaO_3$. The experimental data obtained at different heating rates were analyzed by Friedman analysis and showed a characteristic shape in the plot of energy versus partial area. Further directions of improvement, like improving the densification by sintering, are mentioned in the last section under discussions.

2. Perovskite structure

2.1 Functional Engineering Materials based on Perovskite Crystal structure

The goal of this book chapter is to describe the development of new thermoelectric materials (TE), whose most important features are described first. Then the perovskite structure is reviewed, before focusing on the main topic, $NaTaO_3$.
Successful thermoelectrics have to be semiconductors [Sommerlate et al. 2007, Nolas et al. 2001, Ryan&Fleur 2002, Bulusu et al.2008], so there are two possible approaches in TE development, one from the ceramic side, which have large Seebeck coefficients, and one from the metal side, which have large electric conductivity, but a rather poor Seebeck coefficient. The main goal of development for ceramics, which are the focus in this book, is the improvement of the electric conductivity. The engineering targets of such TE-ceramics are applications in any combustion engines, gas turbines, power plants including nuclear power plants, furnaces, heaters, burners or in combination with solar cells or solar heaters as illustrated in fig. 1.

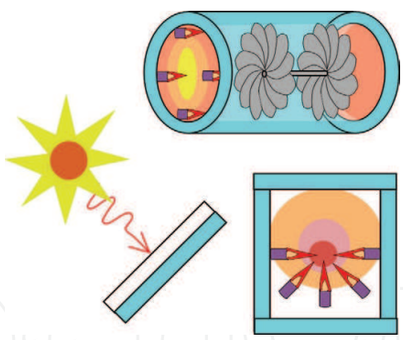

Fig. 1. Possible applications for high-temperature thermoelectric ceramics (in blue color) in solar cells, solar heaters, combustion engines or gas turbines.

The service temperatures of such devices are usually too high as to be applicable for other TE materials. The temperature difference [Ryan& Fleur 2002] between the hot chamber inside and the (cold) ambient environment is considered as the energy source for these energy conversion devices, which have a long life time and low maintenance costs, because there are no rotating parts. The main advantage is that any waste heat can be converted into electricity. Hence, advanced thermoelectrics are both, environment-friendly eco-materials and energy materials, which main purpose is producing energy. For a wide range of applications, materials with higher energy conversion efficiency than present TEs need to be found, in order to be considered as clean energy sources helping to solve the severe CO_2-

problem. One important indicator for efficient thermoelectric material is the figure-of-merit *ZT*

$$ZT=S^2\sigma T/\kappa, \quad (1)$$

which should have a value significantly larger than 1 to be economically reasonable. Improvement of *ZT* requires a high Seebeck coefficient *S* and electric conductivity σ, and a low thermal conductivity *κ*. For increasing *ZT* several concepts for materials design of thermoelectrics have been introduced [Nolas et al. 2001, Ryan&Fleur 2002, Bulusu et al.2008, Wunderlich et al. 2009-c]. These are phonon-glass electron-crystal (PGEC) [Terasaki et al.1997], heavy rattling atoms as phonon absorbers, proper carrier concentration [Vining 1991, Wunderlich et al.2006], differential temperature dependence of density of states, high density of states at the Fermi energy, high effective electron mass [Wunderlich et al. 2009-a], superlattice structures with their confined two-dimensional electron gas [Bulusu et al. 2008, Ohta et al. 2007, Vashaee & Shakouri 2004], and electron-phonon coupling [Sjakste et al. 2007]. As all these factors can influence also the material focused in this chapter $NaTaO_3$, at first basic principles of the Pervoskite crystal structure are briefly reviewed, as this interdisciplinary approach is supposed to gain important understanding for future improvement.

The interest on Perovskite structure related materials has dramatically increased in the past three decades after the discovery of many superior solid-state properties, which makes Perovskite materials or their layered derivatives record holders in many fields of solid state physics as shown in fig. 2. The most popular finding was the discovery of superconductivity in $Y_1Ba_2C_3O_{7-x}$ (YBCO) for which the Nobel Prize 1987 was provided. The present record holder is Bi2212 with a critical temperature of T_C=120K. A large scale application of YBCO since 1998 is the linear motor train using the magnetic levitation (Maglev) in Yamanashi-ken Japan, whose entire rail consists of Helium-cooled superconductors. Present portable phone technology is all based on layered $(Ba,Sr)TiO_3$ dielectric material [Ohsato 2001, Wunderlich et al. 2000] due to their high dielectric constant (e>10000) and quality factor. During the materials development detailed spectroscopic data of the electromagnetic resonance [Bobnar et al. 2002, Lichtenberg et al. 2001] have been measured, which further analysis can provide more understanding of electron-phonon interactions as one of the key issue for thermoelectrics based on perovskites. Piezoelectric materials on $Pb(Ti_{1-x}Zr_x)O_3$ (PZT) or the environmental benign lead free $K_{0.5}Na_{0.5}NbO_3$ (KNN) materials [Stegk et al. 2009] have an increasing application demand in actuators and sensors.

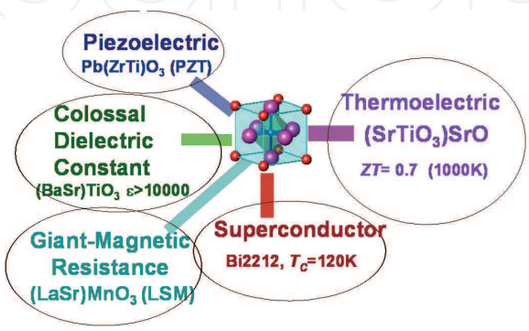

Fig. 2. As Perovskite-structure based mate-rials are record holders in many solid-state properties, they might become so in thermoelectrics too.

The main reason for the good piezoelectric properties with its large d_{33} shear component is that soft modes in the phonon spectrum appear near the morphotrophic phase boundary [Stegk et al. 2009]. This derives from the softening of the atomic bonds by adding other elements, or from increasing of the lattice constants as described in the next sub-section. The Nobel Prize 2007 has been provided for the discovery of the giant magnetic resonance (GMR) observed on Heusler-phases, but it also occurs on Perovskite interfaces as in (La,Sr)MnO_3 [Coey et al. 1999]. Similarly, for thermoelectric materials, like the layered Perovskite-relatives called Ruddlesden-Popper phases $(SrTiO_3)_n(SrO)_m$, large ZT values have been reported.

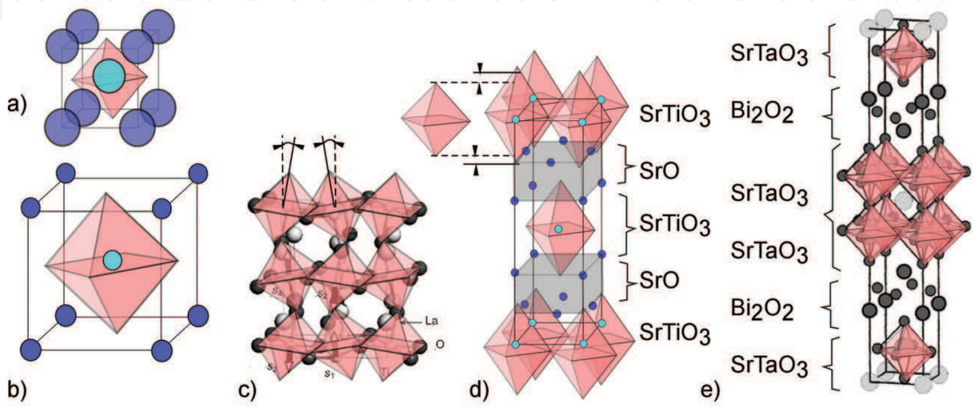

Fig. 3. Schematic drawing of the crystal structure of the perovskite structure and of relatives, (a) perovskite structure with small lattice constant compared to atomic radius, (b) same with large lattice constants, (c) tilted octahedron in $LaTiO_3$, (d) layered Ruddlesden-Popper phase with uniaxial distorted TiO_6-octahedron, (e) Aurivilius phase.

The Perovskite structure is schematically summarized in fig 3. In pure perovskites there are two extreme structural variants, expressed by the tolerance factor f [Imada et al. 1998]

$$f = \frac{r_A + r_O}{\sqrt{r_B + r_O}} \tag{2}$$

where r_A, r_B, r_O are the atom radii or the A-(alkali or rare earth-), B-(transition metal group-elements), and O-atom in ABO_3-perovskites. The first extreme with small f (fig. 3a) has small lattice constants compared to the atomic radii. Thus, the atoms fit almost without free volume into the cubic unit cell. The second variant with large f (fig. 3b) has large lattice constants compared to the atomic radii. Hence, phonon modes especially soft modes can easily be excited and this is considered as a beneficial factor for many of the superior solid-state properties mentioned above [Imada et al. 1998, Stegk et al. 2009]. If the space for the octahedron is too large, they start too tilt as shown in fig. 3 c for $LaTiO_3$. This is considered as bad for the thermoelectric properties. This holds also true for the case of the uniaxial octahedron extension as shown in fig. 3 d for the layered Ruddlesden-Popper phase [Ruddlesden & Popper 1958], which is a natural grown nano-composite consisting of SrO and $SrTiO_3$. They are explained in the section 2.3, as well as the Auirvillius phases (fig, 3 e), but before that the findings on perovskite-based thermo-electrics are briefly summarized.

2.2 Perovskite based thermoelectrics

Focusing from now on thermoelectric materials, it has been shown [Yamamoto et al. 2007, Sterzel & Kuehling 2002] that in the (Sr,Ba,Ca)TiO_3 ternary system only specimens at the Sr-rich corner show a large Seebeck-coefficient. Because pure $SrTiO_3$ is an insulator with a band gap of 3.2 eV, it needs to be doped in order to become a semiconductor. N-doping has successfully been demonstrated by partially substitution of Sr with La, or Ti with Nb, and a rather large thermoelectric figure of merit of 0.34 at 1000K is achieved [Ohta et al. 2005-a,b, Wunderlich et al. 2006] As shown in fig. 4, the principle is the same as doping in Si, electron donator elements from the right side of the host atoms in the period system are substituted. However, in these oxide ceramics, not only an electron is released, but also due to the valence change of Ti-atom, oxygen atoms are released (fig, 4 b). Hence, firing in reduced atmosphere improves the properties of Nb-doped $SrTiO_3$, as well as $NaTaO_3$ as explained later.

The oxygen deficit introduces an additional electronic state 300 mV below the valence band edge, as discussed elsewhere [Wunderlich et al. 2009-a]. In this paper also one of the reasons for the good thermoelectric performance of $SrTi_{1-x}Nb_xO_{3-v}$, has been discovered.

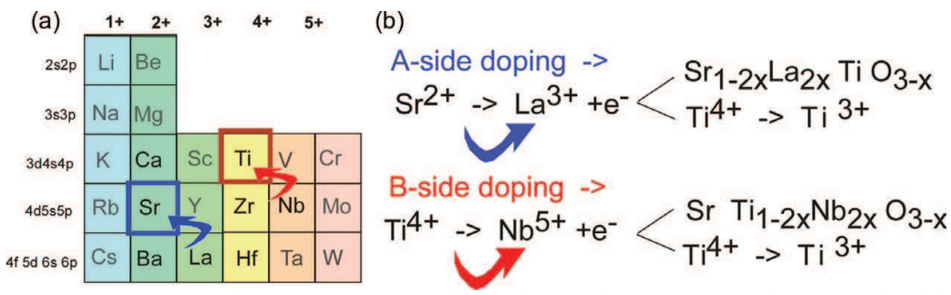

Fig. 4. N-type doping of $SrTiO_3$ for A- and B-side in shown (a) in the period table, (b) as reaction equation with either creation oxygen vacancies or changing the oxidation state of the Ti-atom.

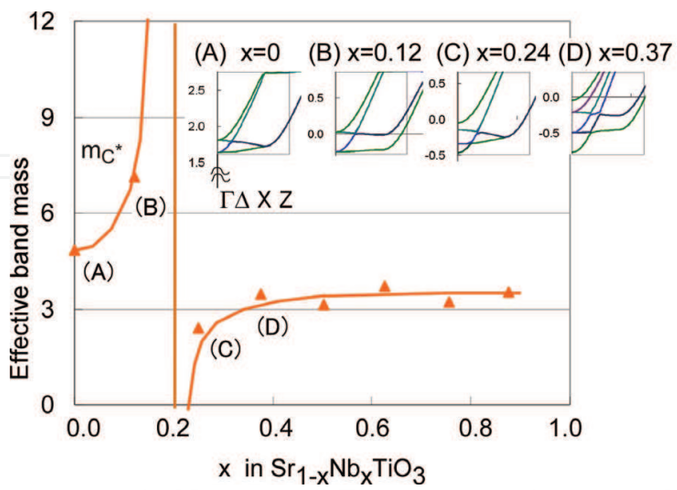

Fig. 5 Effective band mass in Nb-doped $SrTiO_3$ as a function of the Nb-content. The inset shows the conduction band features near the bandgap for different concentrations in Γ-Z direction, from which the effective mass was estimated [Wunderlich et al. 2009-a].

When x, the doping concentration ob Nb increases, the effective electronic mass increases as shown in fig. 5. When analyzing the band structure, this fact can be explained by the decrease in energy of a flat band as seen in the inset of fig. 5. At the concentration of x_{Nb} =0.24 the low-mass band stretching becomes too large and it forms an independent band section at the Γ-point (inset of fig. 5, case (C)). As a result the band mass suddenly becomes small, and in the experiments the bad TE-properties have been confirmed.
The finding expressed in fig. 5 [Wunderlich et al. 2009-a] can be considered as a kind of guideline for any functional material development. In contrary to structural materials, where a wide concentration range gives usual good performance, in functional materials only a narrow concentration range gives good properties. "A little bit increases the performance remarkable, but a little bit too much, deteriorates them", is a principle occurring often in nature, especially in organic or bio-chemistry.
Another reason for the success of Nb-doped $SrTiO_3$-Perovskite has been suggested by the decrease of the bandgap due to phonons [Wunderlich W., 2008-a]. This mechanism explains the importance of phonons for electron excitation as the origin of the heat conversion, and on the other hand it explains the large Seebeck coefficient due to reduction of recombination. Namely, when the excited electron wants to jump back to ground state, the phonon has traveled away and the bandgap is large as it is without phonon making a de-excitation unlikely.
The following formula [Wunderlich et al. 2009-a] relates the calculated band masses to the effective band mass m^* as determined in experiments

$$m^* = m_e^* = m_{B,i} \tag{3}$$

by taking $m_{B,i}$ with i=1, the next band to the band gap from band structure calculations, as an average of high and low band masses $m_{B,i,h}$ $m_{B,i,l}$ at two different reciprocal lattice points by

$$m_{B,i} = \left(m_{B,i,h}^{3/2} + m_{B,i,l}^{3/2} \right)^{2/3} \tag{4}.$$

Through these band mass calculations it was described for the first time [Wunderlich & Koumoto 2006], that $NaTO_3$, $KTaO_3$ and others are possible TE-candidates, because they possess a large effective mass of m^*/m_e=8, about two times larger than Nb-$SrTiO_3$. Before describing $NaTO_3$ in section 2.4., we briefly summarize findings on layered Perovskites.

2.3 Layered Perovskites as thermoelectrics

The electron confinement at Perovskite interfaces has been demonstrated first in [Ohmoto & Hwang 2004]. Due to such 2-dimensional electron gas (2DEG) at interfaces, also thermoelectric properties are enhanced as predicted theoretically (see references in [Bulusu & Walker 2008]). The confined electron gas has been successfully demonstrated for Nb-doped $SrTiO_3$, and this discovery leads to Seebeck coefficients ten times higher than bulk materials [Mune et al. 2007, Ohta et al. 2007, Hosono et al. 2006, Lee et al. 2008]. Theoretical calculations [Wunderlich et al. 2008] showed that the control of the concentration on

atomistic level, diffusion and structural stability is essential, as a $SrTiO_3$-$SrNbO_3$-$SrTiO_3$ composite is much more effective that an embedded Nb-doped $SrTiO_3$.
The idea that an insulating nano-layer of SrO inside Nb-doped $SrTiO_3$ reduces the thermal expansion of the composite, has been demonstrated for the Ruddlesden-Popper phase [Lee et al. 2007-a, Lee et al. 2007-b, Wunderlich et al. 2005], which are naturally grown superlattices [Haeni et al.2001]. As mentioned in section 2.2, in such case structural uniaxial distortions of the Ti-octahedron can occur, which deteriorate the thermoelectric properties due to their larger Ti-O-distance. By additional doping elements the extension can be restored and thermoelectric properties are improved [Wang et al. 2007].
Other Perovskite relatives are the various Aurivilius phases, which consists of Bi_2O_2 layers between Perovskite [Lichtenberg et al. 2001, Perez-Mato et al. 2004]. Their thermoelectric conversion power has yet been tested to a certain degree. Other Perovskite relatives are the Tungsten-bronze crystals [Ohsato 2001], which have not yet been tested.

2.4 Pure $NaTaO_3$ is a distorted Perovskite

The interest in $NaTaO_3$ recently increased after the discovery of its photo catalytic properties as water splitting [Kato et al. 1998], or degradation of organic molecules, especially when doped with rare earth elements like La [Yan et al., 2009]. In spite of its high melting point of 1810°C [Lee et al. 1995, Suzuki et al. 2004] it has a lattice energy of -940 kJ/mol, but not as low as Ta_2O_5 (-1493 kJ/mol). It can be produced at relatively low temperatures from $Na_2C_2O_4$ and Ta_2O_5 [Xu et al. 2005] and it reactives with Si_3N_4 [Lee et al. 1995]. $NaTaO_3$ forms an eutectic ceramic alloy with $CaCO_3$, which lowers the melting point to 813 K [Kjarsgaard & Mtchell 2008]. Ta in $NaTaO_3$ can be exchanged isomorphly by Nb, relating in similar properties as $NaNbO_3$ [Shirane et al. 1954, Shanker et al., 2009].
Detailed investigations showed that $NaTaO_3$ possesses the Pervoskite structure (*Pm-3m*) only above (893 K) before it lowers its symmetry becoming tetragonal (*P4/mbm*), and orthorhombic (*Cmcm, Pbnm*) below 843 K and 773 K, respectively [Kennedy et al. 1999]. $NaTaO_3$ is more stable compared to $NaNbO_3$, which becomes tetragonal at 653 K and orthorhombic at 543 K, or $KNbO_3$, where these transformations occur at 608 K and 498 K, respectively [Shirane et al. 1954]. $NaTaO_3$ has a bandgap of 4eV [Xu et al. 2005]. The phase transition is caused by the octahedron tilting (fig. 2 c), which can reach up to 8° in the case of $NaTaO_3$ [Kennedy. et al. 1999].
$NaTaO_3$ has been suggested as thermoelectric material [Wunderlich & Koumoto 2006, Wunderlich et al. 2009-a, Wunderlich & Soga 2010], as it shows a large Seebeck coefficient. The findings are briefly summarized, together with explanation of new research results in the following sections.

3. *Ab-initio* calculations of doped $NaTaO_3$

First-principle calculations based on the density-functional theory (DFT) are presented in this chapter. They should clarify the following topics, namely which doping element sits on *A*- or *B*-site of the perovskite lattice ABO_3, how the lattice constants change, how Fermi energy and bandgap change, and finally how the bandstructure and density-of-states (DOS) looks like.
The first principles calculations were performed using VASP software [Kresse & Hafner 1994] in the LDA-GGA approximation with a cut-off energy E=-280eV, U=0V and sufficient

number of k-points. The DOS is convoluted with a Gaussian distribution with a FWHM of 0.2eV, to approximate the broadening at room temperature. The relevant symmetry points in reciprocal space were chosen according to the standard notifications of the Perovskite space group *Pm-3m*, which was assumed as a first approximation to have untitled octahedra. The path in reciprocal space was focused on the three directions near the Γ-point, see discussion in [Wunderlich et al. 2009-a]. The supercell used in these calculations is a 2x2x2 extension of the unit cell, allowing calculations of minimal doping concentration steps of 0.125 = 1/8 for *A*- or *B*-side or 1/24 for O.

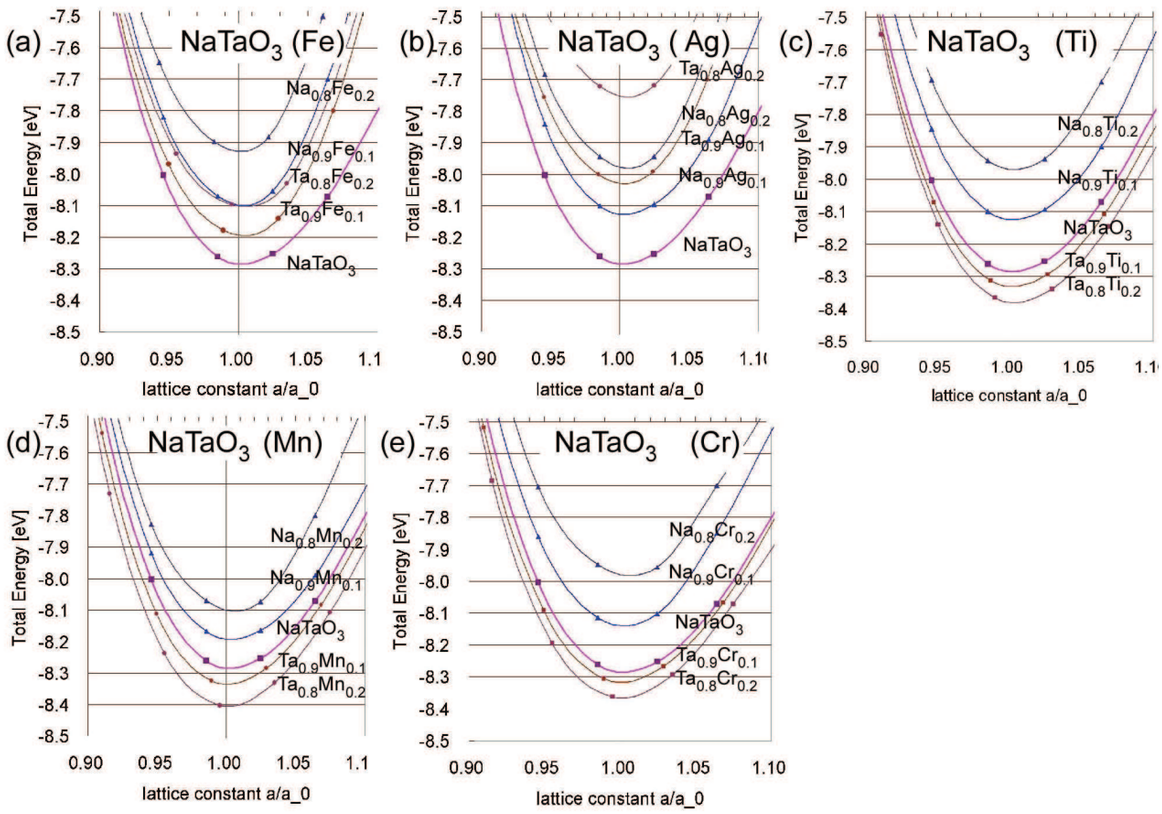

Fig. 6. The energy-volume dependence for pure $NaTaO_3$ (pink line) is shown and compared with different doping elements dissolved in $NaTaO_3$, either on Na- or Ta-side, each for two concentration. The variants with lowest energy are (a) Fe on Ta-side, (b) Ag on Na-side, and (c) Ti, (d) Mn, (e) Cr all three on Ta-side.

Doping element $NaTa_{0.9}Me_{0.1}O_3$	un-doped	Fe	Ag	Ti	Mn	Cr
Lattice constant [nm]	0.3909	0.3948	0.3968	0.3909	0.3952	0.3929
Band-gap [eV]	2.20	0.74	0.60	2.10	0.95	1.30
Fermi energy [eV]	2.37	1.91	1.80	2.17	1.95	2.54

Table 1. Lattice constants, band-gap and Fermi energy for Ta-site doped $NaTaO_3$ as estimated from *ab-initio* calculations

The results of the energy-versus-volume (E(V)) calculations are shown in fig. 6 for doping elements Fe, Ag, Ti, Mn, and Cr for either doping on *A*- or *B*- side. The obtained lattice constants are shown in table 1 and exhibit only a small change compared to pure $NaTaO_3$. As explained in the following section and in a previous paper [Wunderlich 2009-b], Ag and Fe are the two doping elements, which cause the highest Seebeck voltage due to their high solubility in the $NaTaO_3$ lattice. The data in fig. 6 show that both, Fe, and Ag, doped on *B*-site have a slightly higher energy, while according to the experimental data intuitively one would expect a lower energy than pure $NaTaO_3$, as it is in the case for all other doping elements. The discrepancy can be explained by the fact that pure $NaTaO_3$ has tilted octahedron. Furthermore, Ag shows a slightly lower energy for doping on *A*-side, but this makes no sense, because valence and hence band structure remains unchanged. As in the case of Nb-doped $SrTiO_3$ [Wunderlich et al. 2009-a] DFT-calculations of the combined defects $NaTa_{0.88}Me_{0.12}O_{3-x}$ might clarify this issue. As explained in fig. 4 b in the previous section, an increase in the electron concentration on *B*-side is always related to a deficit in oxygen.

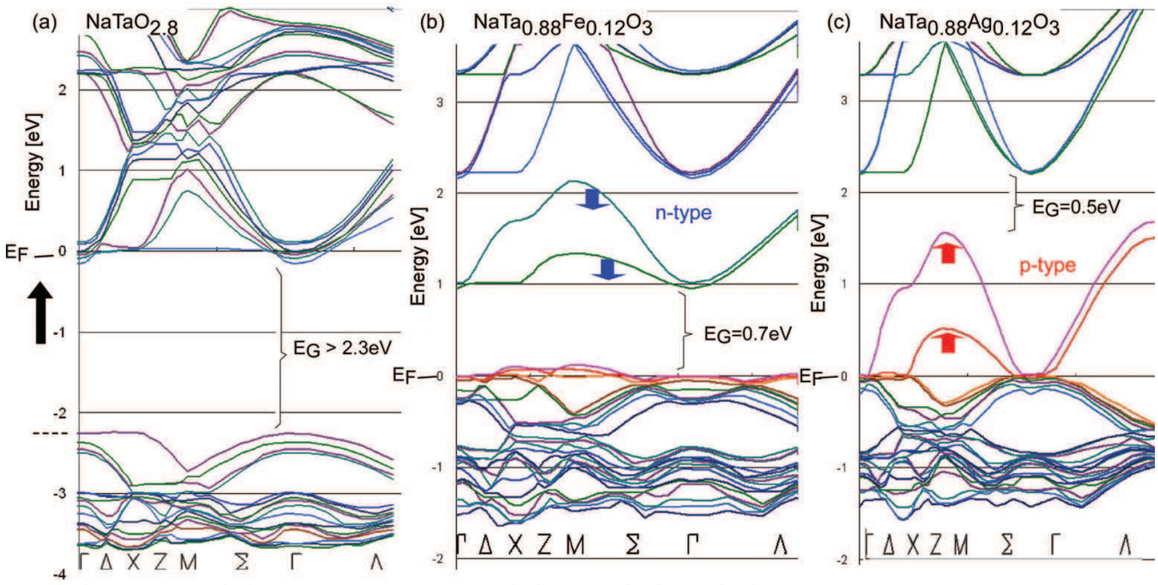

Fig. 7. Band structure of (a) $NaTaO_{2.8}$. (b) $NaTa_{0.88}Fe_{0.12}O_3$ (n-type) (c) $NaTa_{0.88}Ag_{0.12}O_3$ (p-type). The arrows show the change compared to un-doped $NaTaO_3$. (The band colors are just for distinguishing and have no other meaning).

The calculated band structure of Fe-doped $NaTaO_3$ is shown in fig. 7 b, that of Ag-doped $NaTaO_3$ in fig 7 c and the oxygen-deficit $NaTaO_{2.8}$ lattice in fig. 7 a. In all plots the Fermi energy level, which is shown in table 1, has been adjusted to 0 eV. In the case of n-doping the Ta-*2eg* bands have lowered their energy and the band gap is reduced remarkably from 2.2 eV in pure $NaTaO_3$ to 0.74 eV, so that excitations due to phonons become possible. The p-doping by Ag shifts the Ta-*2eg* bands towards the valence band, so that an indirect band gap with 0.6 eV occurs. As shown in table 1, the band structures of other doping elements show larger band gaps. The band gap widths correspond well to the electric resistivity of

such specimens as explained in the next section. Hence, the band-gap-reduction will be a future engineering challenge for obtaining a large electric conductivity.

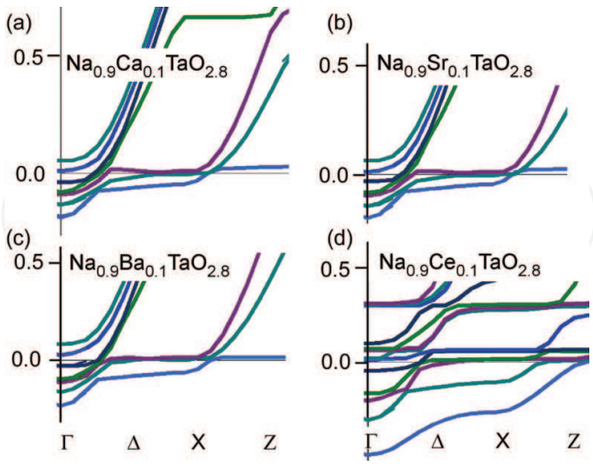

Fig. 8. Band structure near the conduction band edge at the Γ-point for Na-site doping, (a) $Na_{0.88}Ca_{0.12}TaO_{2.8}$, , (b) $Na_{0.88}Sr_{0.12}TaO_{2.8}$, (c) $Na_{0.88}Ba_{0.12}TaO_{2.8}$, , (d) $Na_{0.88}Ce_{0.12}TaO_{2.8}$.

The mechanism for electron conductivity is similar to that in Nb-doped $SrTiO_3$; for details see the discussions in [Wunderlich et al. 2009-a]. The oxygen vacancies introduce electronic states about 200 ~ 300 meV below the valence band edge, form which electrons from the conduction band can be excited into the valence band. Compared to pure and Nb-doped $SrTiO_3$ (m^*/m_0= 4.8 and 8), in pure $NaTaO_3$ (m^*/m_0= 8) the effective electron mass increases further (m^*/m_0= 12), as can be seen from the flat bands over the entire region Γ–Δ-X in all three cases of fig. 7. In un-doped $NaTaO_3$ the hole mass is also large (m^*/m_0= 8). The mass of Ag-doped $NaTaO_3$ (Fig. 7 c) is smaller due to the indirect bands at Z and Λ-points, but the large effective mass of the valence band minimum in un-doped regions (m^*/m_0> 20) seems to have also an large influence on the effective mass measured in experiments. Calculations for A-site doping analog to La-doped $SrTiO_3$ [Wunderlich et al. 2009-a] are shown for $NaTaO_{2.8}$ in fig. 8. In all cases the DOS near the band edge is increased, but for Ce-doping it became especially large as can be also seen on the increased number of bands (fig. 8 d). In spite of experimental difficulties with sintering of Ce_2O_3 containing samples [Wunderlich et al. 2009-d], a large TE-performance by co-doping might be expected. In following experimental results about Ta-site doping are reported.

4. Specimen preparation and microstructure characterization of $NaTaO_3$

$NaTaO_3$ composite ceramics were produced by conventional sintering. Well-defined weight ratios of fine powders of $NaTaO_3$ (Fine Chemicals Ltd.) and each of the pure metals Fe, Ag and other metals, or Fe_2O_3, were mixed in different concentration ratios in a mortar for more than 10 min. The specimens were pressed with 100 MPa as pellets, 10 mm in diameter and 3 mm height, and sintered in a muffle furnace in air at 1000 °C for 5h with slow heating and cooling rates (50K/h) as sketched in fig. 9. The electric properties of the specimens were analyzed as explained in the following section. Thereafter, the sintering was repeated several times at the same temperature. During sintering the white color of $NaTaO_3$

specimens turn into dark colors indicating that the band-gap has been reduced, when a large amount of metals was dissolved. However, specimens containing metals with low solubility such as Al, Cu, Sn, Sb, Mo, W remained white or turned into light orange or reddish color (Ti). The specimens were characterized by SEM (Hitachi 3200-N) at 30kV equipped with EDS (Noran), which allows chemical mapping. The X-ray diffraction (XRD) analysis was performed using a Rigaku Miniflex device with Co-source with 1.7889 nm wavelength. Simulation of the XRD-patterns was performed with the Carine V3 software (Cristmet).

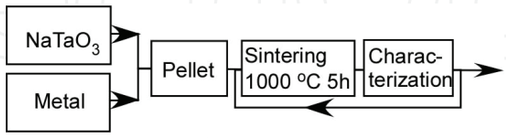

Fig. 9. Flowchart of the specimen preparation

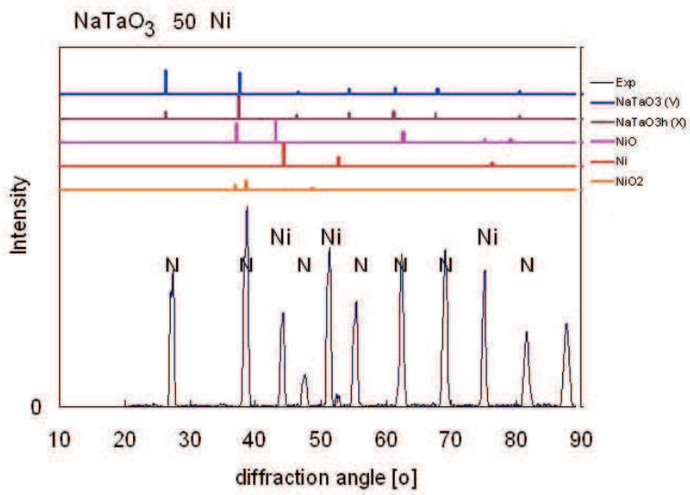

Fig. 10 XRD diffraction pattern of $NaTaO_3$ with 50 wt-% Ni. The letters N indicate $NaTaO_3$ reflexes.

The analysis of XRD-diffraction pattern of Fe- and Ti-doped $NaTaO_3$ showed [Wunderlich, Soga, 2010] that the initially mixed Fe or Ti-metallic powder gets oxidized as besides the $NaTaO_3$- XRD-peaks also such of FeO_3- or Ti_2O_3 are observed. Hence, during sintering a FeO_3- and Ti_2O_3–$NaTaO_3$ composite material is formed by reaction bonded sintering (RBS), a mechanism, which supports additional energy for sintering and has been successfully applied for many structural ceramics [Claussen et al. 1996]. Weight measurements of specimens before and after sintering confirmed the oxidation by weight gain even in quantitative manner.

In the case of Ag, evidences for oxidation have not yet been clearly approved, instead, cooling down a sintered specimen, metallic silver balls separated on the specimen surface are observed. In the case of Ni-added $NaTaO_3$, in spite of the greenish specimen surface color due to NiO, the XRD pattern in fig. 10 shows that the interior of the specimen consists of a composite $NaTaO_3$ with metallic Ni. In all specimens with Fe-, Ni-, Mn-, and Ag-doping the XRD peaks were indentified as Perovskite with space group *Pm-3m* as mentioned in

section 2.4. Hence, it can be concluded, that the octahedron tilting mentioned in section 2 was suppressed by the doping.

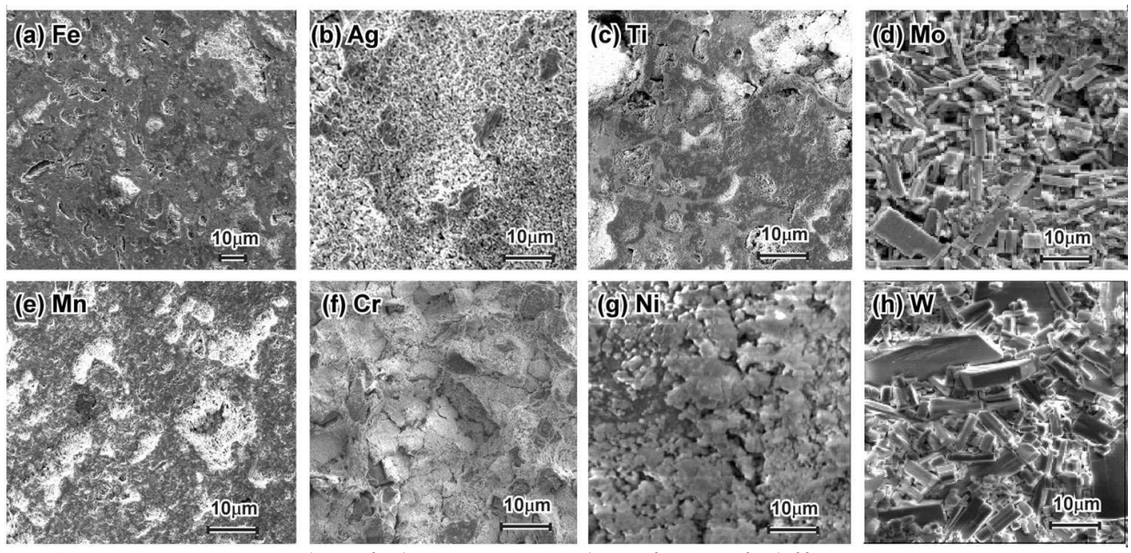

Fig. 12. SEM micrographs of the as-prepared surfaces of different $NaTaO_3$-composites processed by adding 40 wt% of (a) Fe, (b) Ag, (c) Ti, (d) Mo, (e) Mn, (e) Cr, (g) Ni, (h) W.

The microstructure of the $NaTaO_3$ composite processed with 50 wt% Fe consists of a $NaTaO_3$- 50 mol% Fe_2O_3 composite as shown in fig. 12 a. It consists of dark Fe_2O_3 particles, on average 10 μm in size, and appearing in streaks-like shape, which are embedded in a grey $NaTaO_3$ matrix. Detailed explanation is provided in a previous paper [Wunderlich & Soga 2010]. When $NaTaO_3$ is initially processed with Fe_2O_3 instead of Fe, the microstructure looks like a sintered ceramic composite with white Fe_2O_3 besides white $NaTaO_3$ particles. The change from black to white color can be explained by oxygen saturation as explained in section 6. Such a micrograph is shown in a previous paper [Wunderlich 2009-b]. The white areas in fig. 12 a are pores remaining from insufficient compaction during sintering or from released oxygen as explained in section 5.

In $NaTaO_3$-composites containing Ag, Ti, Mn, and Ni the dark, metallic particles are slightly bigger (5~10 μm). The particles have a volume fraction of about 30% which correspond well to the intensity ratios of the XRD-pattern. In specimens, which were produced from Fe_2O_3- instead of Fe-powder, the Fe_2O_3-particles form round particles as shown in fig. 3 a in [Wunderlich 2009-b]. In the case of Cr the dark, metallic Cr-particles are significantly larger (20 μm), which can be explained by their low diffusivity. The same would be expected for Mo and W with their high melting points, but instead they lead to faceted interfaces. By chemical mapping homogeneous distribution of Na, Ta, Mo or W was confirmed. The two elements, Mo, and W, having their location in the period system and their atomic radii close to Ta, and, hence, can inter-diffuse easily with Ta. They lower the surface energy of certain crystallographic planes, which is an important fact to be kept in mind when nano-layered composite materials based on $NaTaO_3$ are desired.

The main goal of doping is to increase the carrier concentration of $NaTaO_3$ in order to increase the conductivity. In a composite this can only be achieved by increasing the concentration of the dissolved element. Composition measurements by EDX in SEM with

lateral resolution of 1 μm were performed on the $NaTaO_3$-phase in the $NaTaO_3$-composites processed with different metals. For Cr, Mo and W concentrations below 2 at% were detected, for Ag, Ti, Mn, and Ni, 5 ~ 10 at% were detected and for Fe 14 at%. This result can Is a necessity for a thermoelectric material and explains the success of Fe and Ag for the TE-performance as explained in the following section.

5. Thermoelectric characterization

5.1 Measuring device

The thermoelectric measurements were performed with a self-manufactured device as shown in the inset of fig. 13. The specimen was attached to the device, so that its left side lies on a copper block as a heat sink and its right side on a micro-ceramic heater (Sakaguchi Ltd. MS1000) with a power of 1kW, and was heated up to 1000°C within 3 minutes. Hence, the bottom part of the specimen experienced the large temperature difference, while the upper part was heated through the heat conductivity of the specimen. The temperature distribution as measured by thermocouples is shown in fig. 1c of [Wunderlich & Soga 2010]. Seebeck voltages were measured on both, the bottom and top part of the specimen by Ni-wires, which were connected to voltmeters (Sanwa PC510), marked as V1 and V2 in the inset of fig. 13 b. The temperature was measured with thermocouples also attached to voltmeters. The data were recorded online by a personal computer.

Most TE-literature reports TE-data measured under small temperature gradient [Bulusu & Walkner 2008], where the theory is valid for. Our device however, measures the data under large temperature gradient, which is close to applications. When comparing such measured data with literature data on similar specimens (CoTiSb, Fe), in general about 1.5 times larger values for the Seebeck voltages are obtained.

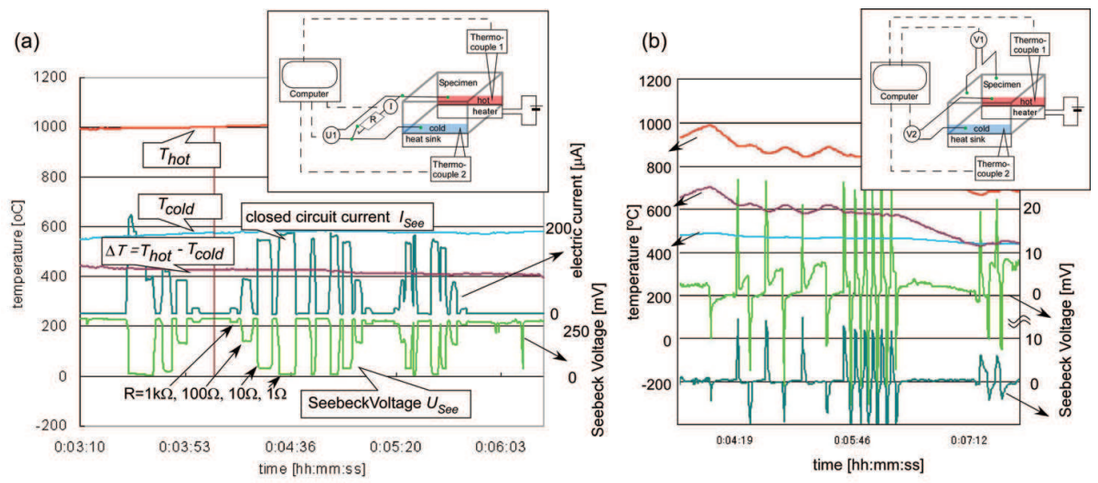

Fig. 13. Temperature (on the left y-axis), Seebeck Voltage and short-circuit current (both on the right y-axis) as a function of time. The inset shows the scheme of the experimental setup for measuring the Seebeck voltage and the closed circuit current. (a) Typical measurement for $NaTaO_3$ + 50 wt% Fe, (b) Seebeck voltage response for $NaTaO_3$ + 50 wt% Cu, when the heater is switched off or on (red line).

By putting the specimen completely above the ceramics heater, the temperature dependence of the electric resistivity was measured with the same device as shown previously [Wunderlich 2009-b, Wunderlich & Soga 2010]. The reason, why the Seebeck voltage only appears when heated above 500°C, can be explained by the poor electric conductivity at low temperatures. The room temperature resistivity of such samples decreases from about 10 MΩ to 0.1 MΩ when sintered in at least five sintering steps (1000°C, 5h) [Wunderlich & Soga 2010]. The temperature dependence of the resistivity ρ was measured. The activation energy E_A for thermal activation of the charge carriers n_e in this n-doped semiconductors was estimated according to $n_e = N \exp(-E_A/2kT)$ by a suitable data fit. This analysis yield to an activation energy for charge carriers of about 1 eV during heating and 0.6 eV during cooling [Wunderlich 2009-b].
Another option of this device is the measurement of the closed circuit current. For this option, the wires below the specimen are connected with resistances of 1Ω, 10Ω, 100Ω, 1kΩ, or 1MΩ in a closed circuit condition as seen in the inset of fig. 13 a. As the measured electric current is a material dependent property, it is recorded too. As shown in fig. 13 a or fig. 3 in [Wunderlich 2009-b], as soon as the circuit is closed, the voltage of the $NaTaO_3$- 30mol% Fe_2O_3 specimen drops down, and the current increases according to the amount of load with a short delay time of a few ms. The detection limits are about U=1mV and I=0.8μA.

5.2 Time-dependence of Seebeck voltage

For the most specimens, the Seebeck voltage is not time-dependent and only depends on the temperature gradient. Time-dependent effects of the Seebeck-voltage occurrence have been reported for Co-based rare-earth Perovskite-composites (for example Gd_2O_3+CoO_x) [Wunderlich & Fujizawa. 2009-d] and were explained as a combined occurrence of pyro-electricity and thermoelectricity. In some Co-based perovskite specimes remarkable non-linearities in the plot Seebeck voltage versus temperature difference appear, but not in $NaTaO_3$.
A time-dependent Seebeck voltage behavior appears at specimens $NaTaO_3$ + x Cu, with x from 30 to 50 wt%, as shown in fig. 13 b for x= 50wt%. On such specimens in general only a small Seebeck voltage of only -5 mV is measured, even at temperatures above 500 °C, when a sufficiently high charge carrier concentration is reached. However, when then the heater is switched off suddenly, a sharp pulse, a few milliseconds in length, of the Seebeck voltage with a value of 20 mV is measured with a negative sign. When switching on the heater again, the sign reverses to a positive pulse of Seebeck voltage with the same absolute value of 20mV. The Seebeck voltage on the backside of the specimen, which experiences the temperature gradient only indirectly through heat conduction, is not so high in its absolute value (12 mV for a 5 mm thick specimen), but it appears with the same sign and at the same time. In fig. 13 b this is shown in dark-green, while the pulse of the specimen side with the large temperature gradient is shown in light-green. The value of the Seebeck pulse is independent on the time-interval between the heat flow reversals, just the Seebeck voltage between the pulses fluctuates between 2 and 10 times of its absolute value. Only when the temperature gradient decreases (right side of fig. 13b), the absolute value of the pulse becomes smaller.
This heat flow dependent Seebeck pulse in time appears also in $NaTaO_3$ + x Ag specimens, which were sintered only for a short time (1000°C, 5h). The reason is not yet completely investigated, but the interface between $NaTaO_3$ and metallic particles, which are not reactive with $NaTaO_3$, is responsible for this effect. It is different from pyroelectricity, which showed a similar behavior like an electric capacitor. The heat-flow dependent Seebeck voltage pulse

can be utilized for building a heat-flow meter, which would be able to detect the forward or backward direction of the heat flow, due to the sign of the voltage pulse. By micro fabrication several such specimens could be arranged under different angles to heat flow, so that the vector of the heat flow can be determined, and when such devices are arranged in an array, even the heat flow tensor can be measured.

5.3 Seebeck voltage measured under large temperature gradients

The measurements of the Seebeck voltage U_{See} are shown in fig. 14, where a temperature gradient of up to ΔT = 800 K was applied to the specimens and the Seebeck voltage measured as explained in section 5.1. The specimens with $NaTaO_3$+x Fe were measured for x = 30, 40, 50, 60, 70, 80, 90 wt%. The specimen with x= 50, 60, 70 wt% showed the high Seebeck voltages of about -300 mV as shown in fig. 14 a, details are explained in previous publications [Wunderlich 2009-b, Wunderlich & Soga 2010]. From the plot temperature difference dT versus Seebeck voltage U_S a Seebeck coefficient S of 0.5 mV/K was estimated by the slope $S = dU_S/dT$.

As the XRD results showed the formation of Fe_2O_3, also $NaTaO_3$ + r Fe_2O_3 specimens were sintered, were r was 30, 50, 70, 90 wt%. These specimens showed all a Seebeck voltage of +60 mV at ΔT = 800K with a slightly nonlinear ΔT-dependence. Hence, different processing causes a different oxidation state of the second component in this composite, and changes the n-type $NaTaO_3$+x Fe into a p-type $NaTaO_3$ + r Fe_2O_3 composite. As mentioned above, the microstructure looks slightly different for both composites and the thermo-kinetic measurements in section 6 too.

When metallic Ni is added to $NaTaO_3$, the sintered composites with x= 30 wt% Ni showed the highest value of -320 mV with a Seebeck coefficient of 0.57 mV/K, as shown in fig. 14 b. In this case non-linear behavior at ΔT = 650 K during heating, and ΔT = 600K during cooling appears at all Ni-specimens, but not at other elements, and is probably related to some phase transitions. In the case of W additions to $NaTaO_3$ the specimens showed only a small Seebeck voltage of -30 mV for all concentrations in the range 30 to 90 wt% (fig. 14 c). A similar behavior is seen for Mo, where the 50 wt% sample showed a Seebeck voltage of -10 mV during heating and +10 mV during cooling. The plots of Seebeck voltage versus temperature difference are linear.

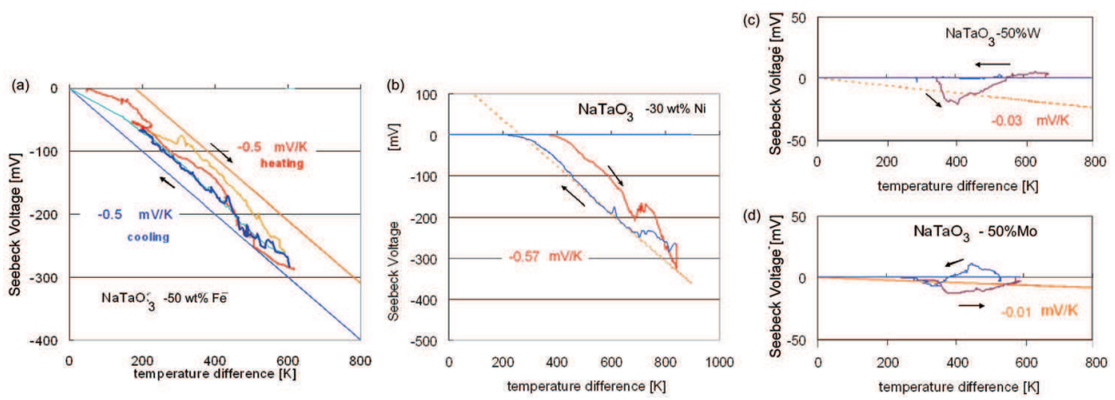

Fig. 14. Seebeck Voltage as a function of the temperature difference for (a) $NaTaO_3$+50 wt% Fe, (b) $NaTaO_3$+30 wt% Ni, (c) $NaTaO_3$+50 wt% W, (d) $NaTaO_3$+50 wt% Mo. The slope of the plots yield to the Seebeck-coefficients as mentioned.

Na --	Mg /	/										Al 0	Si /	P /
K * -30	Ca /	Sc /	Ti -20	V /	Cr -200	Mn -30	**Fe** **-320**	Co -20	Ni -360	Cu -20	Zn /	Ga /	Ge /	As /
Rb /	Sr /	Y /	Zr /	Nb /	Mo -10/+10	Tc /	Ru /	Rh /	Pd /	**Ag** **+250**	Cd /	In /	Sn 0	Sb 0
Cs /	Ba /		Hf /	Ta --	W -20	Re /	Os /	Ir /	Pt /	Au /	Hg /	Tl /	Pb /	Bi 0

* $KTaO_3$+Fe

Fig. 15. Part of the periodic table showing the elements which were tested as doping additives for $NaTaO_3$. The vale refers to the Seebeck voltage in mV at ΔT = 750K. In the case of K it means $KTaO_3$ with Fe-additions. Only the two elements in bold letters (Fe, Ag) showed a remarkable closed-circuit current.

Such measurements were performed by adding several metallic elements *Me* from the periodic system $NaTaO_3$+x *Me* specimens with x = 30, 50, 70, 90 wt%. Fig. 15 shows the largest Seebeck voltage at ΔT=800 K among these specimens, where the best results usually were achieved for x around 50 wt%. Al and those semiconducting elements which were measured did not dissolve in $NaTaO_3$ and such specimens remain white, a sign that they are still insulators.

Specimens sintered from $NaTaO_3$- x Ag powders with x= 30, 50, 60 wt% lead to p-type thermoelectrics. The Seebeck coefficient as deduced from fig. 14 a, Fe as n-type, and the corresponding plot for Ag as p-type [Wunderlich 2009-b] yield for both composites to almost the same value, namely +/- 0.5mV/K. In the case of $NaTaO_3$ + x Fe specimens, the Seebeck voltage increases during the first three sintering cycles (1000 ^{o}C 5h), and reached this saturation value, which was confirmed to be stable even after eight sintering cycles. In the case of Ag-doped $NaTaO_3$, the value also increases, however, after the fourth sintering cycle the Seebeck voltage drops to less than 30mV and the color turns into white again, indicating a structural instability of the $NaTaO_3$-Ag compound probably due to silver evaporation. The temperature dependence of the electric resistivity was shown previously [Wunderlich 2009-b, Wunderlich & Soga 2010] for both, n- and p-type specimens, with x= 50 wt%, which was found as the optimum concentration for low resistivity. According to the thermal activation of the carriers an activation energy in the order of the band gap (1 eV) can be estimated by fitting the data as shown in [Wunderlich 2009-b, Wunderlich & Soga 2010] by the formula $\sigma = N_0 \exp(-E_0/2kT)\ |e|\ \mu_e$. with E_0 activation energy.

There are further promising doping candidates, not yet checked, as Nb, or rare earth. As a conclusion, it can be stated that only the light transition metals like Fe, Cr, Mn, Ni showed remarkable Seebeck voltages. Among them, the closed-circuit measurements described in the following section, lead to further restrictions.

5.4 Electric current under closed circuit conditions

For power generation the performance under closed circuit conditions is important. Fig. 16 shows the measured current when different electric resistances as load are connected. While both composites, the one processed from $NaTaO_3$+x Fe and the $NaTaO_3$- x Ag one, showed

large Seebeck voltage in the range of x = 50 to 70 wt%, the closed circuit current measurements showed the highest value only for the specimen processed from $NaTaO_3$+x Fe with x= 50 wt%, which corresponds to $NaTaO_3$+r Fe_2O_3 with r = 32 mol% after sintering.
In the silver added composite, the specimen with 40 mol% Ag (about 50 wt%) yields to the optimum between large Seebeck coefficient and low resistivity. For the $NaTaO_3$-x Fe_2O_3-composite, the specimen with x = 32 mol % shows the highest current of 320 µA, but for the

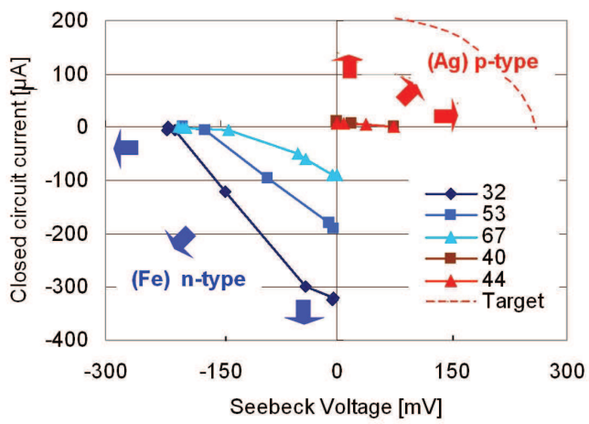

Fig. 16. Seebeck Voltage and closed circuit current for n- and p-type $NaTaO_3$ with Fe- or Ag-additions with the Mol-% as shown. The horizontal and vertical arrows indicate the target for current and voltage increase, the inclined ones indicate the target for power improvement. P- and n-type materials should have the same Seebeck voltage as expressed by the target-line.

$NaTaO_3$-x Ag-composite, it is only 1.2 µA. For the silver added composite, a part of Ag gets dissolved, another part gets oxidized as $NaTa_{1-x}Ag_xO_{3-y}$ + *t* AgO_u, when sintered in three cycles (1000 °C 5h). While $NaTaO_3$- Fe_2O_3 is a stable composite, the metallic Ag in the p-type composite with its low melting point decomposes into an insulating oxide after four sintering cycles (1000 °C, 5h), and metallic silver balls at the surface.
The microstructure of the p-type material needs to be stabilized and optimized for improving both, Seebeck voltage as well as resistivity. When this is realized, and the p-type material would have had the same short-circuit current as suggested by the target line in fig. 16, it is expected that modules with both n- and p-type materials work optimal. As p- and n-type material has been found, $NaTaO_3$ is suggested as a new thermoelectric for power generation suitable for applications in an upper range of application temperatures (500 to 1100 °C), when a sufficient performance is achieved as described in the next section.

5.5 Estimation of the figure-of-merit

The absolute value of the negative Seebeck Voltage increases linearly with the temperature and reaches -320 mV at a temperature difference of 800 K as shown in fig. 14 a for the specimen $NaTaO_3$-50mol% Fe_2O_3. From the slope of the Seebeck voltage versus temperature a Seebeck coefficient of -0.5 mV/K was estimated. Specimens in the range of 20 mol to 70 mol% Fe_2O_3 showed all a Seebeck coefficient larger than -0.45 mV/K. From these data the figure of merit can be deduced, a little bit more promising as previously [Wunderlich 2009-b]. For the thermal conductivity in the worst case a high value of 5 W/(m K) was assumed

according to the range of usual ceramics. This leads to an estimation of the figure-of merit ZT at 1000°C as:

$$Z = \frac{S^2 \cdot \sigma}{\kappa} = \frac{(0.5\,mV/K)^2 \cdot 1\ \mathrm{S/m}}{5\ W \cdot m^{-1} \cdot K^{-1}} = 10 \times 10^{-9}\ K^{-1}, \quad ZT_{1000'C} = 1.27 \times 10^{-5} \tag{5}$$

This estimated value of ZT is at the moment much lower than state-of-the-art materials, for example SiGe, or the above mentioned Nb-doped $SrTiO_3$, but materials development, like improved sintering, higher solubility of Fe, higher conductivity etc., will definitely increase the performance of $NaTaO_3$, for which the following thermokinetic investigations are helpful.

6. Thermo-kinetic characterization

In order to clarify the sintering behavior of the $NaTaO_3$-Fe_2O_3 composite differential scanning calorimetry (DSC) and thermo-gravimetric (TG) measurements were performed. The development in the field of thermo-kinetics in the last decade allows the estimation of activation energies for chemical reactions, when DSC and TG are measured simultaneously with at least three different heating rates [Opfermann et al. 1992, Opfermann 2000]. The analysis of the different sintering steps of alumina [Baca et al. 2001], and the oxidation of Magnetite to Fe_2O_3 [Sanders & Gallagher 2003] are examples, where this technique has successfully been applied for ceramics.

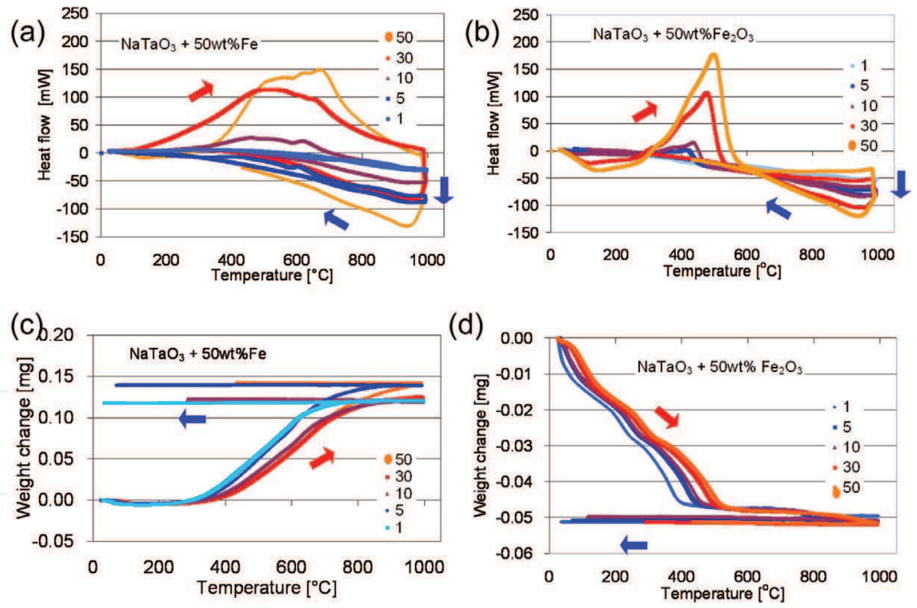

Fig. 17 Results of (a,b) DSC and (c,d) TGA measurements of (a,c) $NaTaO_3$ + 50 wt% Fe-, and (b,d) $NaTaO_3$ + 50 wt% Fe_2O_3-powder specimens. The numbers in the inset refer to heating rates in [K/min]. The red and blue arrows indicate heating and cooling, respectively.

Simultaneous DSC-TG measurements were performed on a SDT Q600 (T.A.instruments) by heating two different sets of mixed powder samples (26 mg $NaTaO_3$ + 50 wt% Fe, and 60 mg $NaTaO_3$ + 50 wt% Fe_2O_3) under air with five different heating rates up to 1000 °C. The

results are shown in fig. 17. The thermo-gravimetric measurements showed that the $NaTaO_3$-50wt% Fe powder gains 0.13 mg in weight (fig. 17c, increase of 0.5%) and the $NaTaO_3$-50wt%Fe_2O_3 powder looses 0.05 mg in weight (weight reduction of 0.2%). The fact that the weight gain in fig. 17c is not the same for all heating rates can be explained by concentration inhomogeneities in each specimen.

The interpretation of these results is that Fe gets oxidized forming Fe_2O_3 which was observed in the XRD pattern, see section 4 and [Wunderlich & Soga 2010]. The experimental results showed that a part of Fe gets dissolved in $NaTaO_3$, about 14 %. Assuming that the same amount of Fe is dissolved in $NaTaO_3$ in both composites ($NaTaO_3$ + 50 wt% Fe and $NaTaO_3$ + 50 wt% Fe_2O_3), this fact can explain why the weight decreases for the $NaTaO_3$ + Fe_2O_3 mixture. Namely, the dissolved Fe needs to be reduced from the initial Fe_2O_3 and the excess oxygen is released.

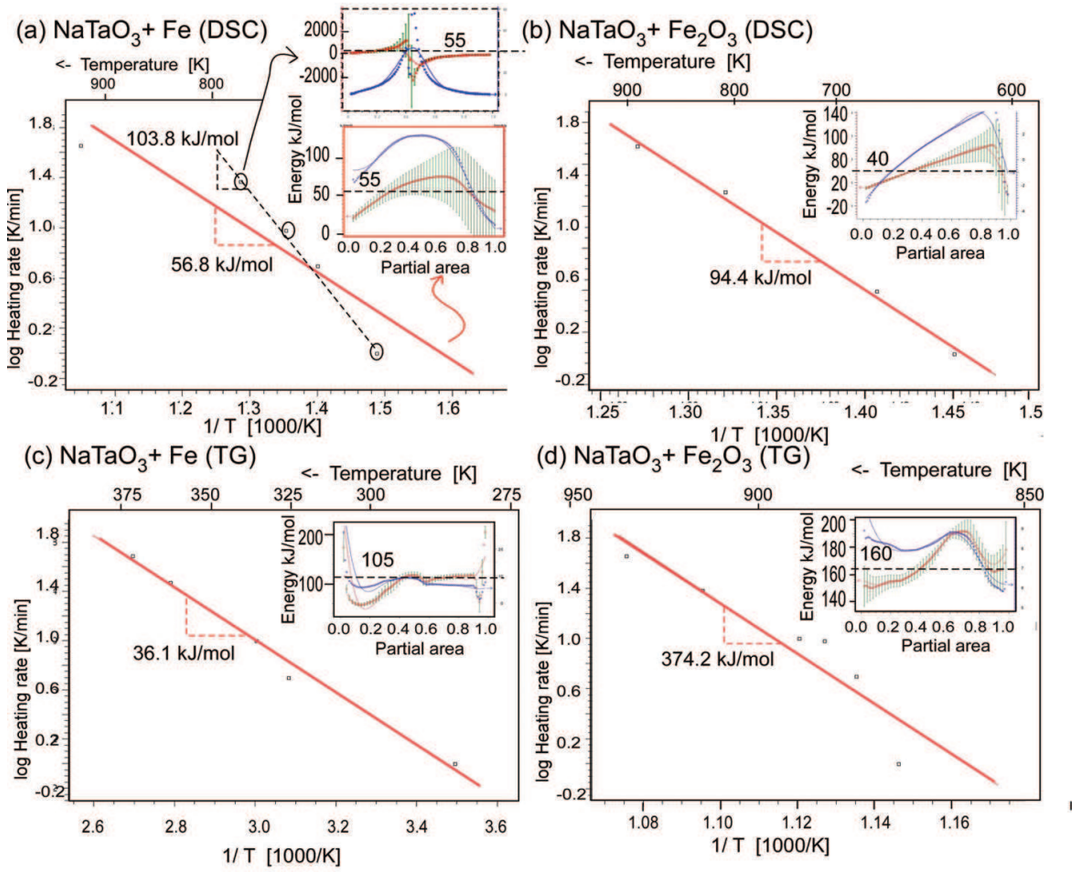

Fig. 18. Analysis of the (a,b) DSC-, (c,d) TG-data from fig. 17 for (a,c) $NaTaO_3$ + 50 wt% Fe and (b,d) $NaTaO_3$ + 50 wt% Fe_2O_3 using ASTM and Friedman method yielding to the activation energy from the slope in the logarithmic plot heating rate versus inverse temperature. The inset shows the distribution of the activation energy as a function of the partial fraction.

The DSC measurements showed an exothermic peak for $NaTaO_3$ + 50 wt% Fe (fig. 17 a), namely a positive heat flow, with a broad maximum at 500°C and small wiggles at 690 °C

and 700 °C, present in data obtained at all heating rates at the same temperature. On the other hand, at the $NaTaO_3$-Fe_2O_3 mixture the main exothermic peak shifts from 410 °C at slow heating rates (1 K/min, 3 K/min) to 510 °C at the fastest heating rate (50 K/min). At these temperatures the corresponding TG-data showed a large decrease in weight, indicating a chemical reaction.

The Netzsch Thermokinetics software package version 3 [Opfermann 2000] was used for data analysis. All four sets of data were analyzed separately and only the data during heating were used. For each set, the parameter-free analysis of the activation energy according to ASTM E698 was performed as shown in fig. 18. Then Friedman analysis [Opfermann et al. 1992, Opfermann 2000] of the activation energy as a function of the partial area was performed as shown in the insets of fig. 18.

The results show an activation energy of 56.8 kJ/mol for the $NaTaO_3$ + 50 wt% Fe- specimen (fig. 18a). The activation energy increases to 103.8 kJ/mol, when only the three data points with best correlation are used, as shown with the circles. In this case the Friedman analysis yields a curve, which looks in its shape like a resonance curve (inset of fig. 18a, upper part, fig. 5). As a function of partial area the energy increases to a partial area of 50%, then suddenly drops down and increases asymptotically. The pre-factor a of the logarithm shown in blue in the inset of fig. 18a has a maximum at the transition point at the partial area 0.5.

The activation energy of DSC of the Fe specimen (fig. 18a) is estimated as 118.4 kJ/mol, when also the fourth data point with good matching is included. This energy is exactly the formation enthalpy for Fe_3O_4 magnetite, but concerning the oxidation states (0, +2, +3, +4), the sequence is [Majzlan et al.2004]:

$$Fe - FeO\ (-266.3\ kJ/mol) - Fe_2O_3\ (-824.2\ kJ/mol) - Fe_3O_4\ (-118.4\ kJ/mol) \quad (6)$$

Such a change in oxidation state is impossible, and the formation of Fe_3O_4 magnetite is unlikely; instead, the formation of FeO could explain the change of the color from white to black for the $NaTaO_3$ + Fe composite and from brown to black for the $NaTaO_3$ +Fe_2O_3 composite. The XRD spectrum, which was measured on bulk specimens, however, showed only evidence for the presence of Fe_2O_3. Also, the other activation energies (fig. 18 c, d) do not fit to the mentioned sequence. The small activation energy of 36 kJ/mol estimated from TG on Fe is explained by the solution of Fe into the $NaTaO_3$ lattice. The Friedman analysis of this data shows the smoothest fit, almost constant energy for the entire region of the partial area (inset of fig. 18b).

As summarized in the following section, the sintering behavior of the $NaTaO_3$-Fe_2O_3 composite produced from Fe or Fe_2O_3 is a combined reaction between Fe-solution in the Perovskite lattice, the oxidation of Fe and the reaction bonding, so the quantitative analysis of the DSC and TG data remains a challenge, but some preliminary suggestions are made during the following discussion.

7. Discussion: Micro-structural and electronic model of $NaTaO_3$

In this section the above mentioned data are discussed and ideas for further development are provided. A detailed understanding for the reaction behavior and thermoelectric properties of $NaTaO_3$ + Fe composite would provide the opportunity to increase its performance. Two facts are obvious and should be tried first. The first task is to improve the

sintered density as the present material still contains pores (fig. 12). The next step is the increase in electric conductivity, which is considered as the main factor for the poor figure-of-merit. Thereafter, the Ag-doping need to be stabilized.

The quantitative explanation of the doping requires detailed understanding of the defect chemistry of iron oxides and Perovskites and is still a challenge. In the following, we present a suggestion for the coupled reaction equation, where the quantitative values are more or less rough estimations. $NaTaO_3$ sintered with Fe reacts in the following way to the n-type composite:

$$NaTaO_3 + x\,Fe \rightarrow NaTa_{1-x}Fe_xO_{3-y} + y\,O + 2x\,e^- \quad \text{with } x = 0.14,\ y = \sim 2/3\,x \tag{7}$$

$$z\,Fe + (y + w)\,O \rightarrow (z-x)/2\,Fe_2O_{3-u} \qquad \text{with } u = f(v, w, y, x, z) \tag{8}$$

where z is the molar ratio of the amount of $NaTaO_3$ relative to Fe in the mixed powder specimens before sintering. y is the estimated amount of oxygen released by the reduction of $NaTaO_3$ when Fe is dissolved, which gives two electrons and releases instead one of the three oxygen atoms. The value of x=0.14, maximum solubility of Fe in $NaTaO_3$, is an experimental result of the SEM-EDX analysis (section 4). w the weight gain in oxygen taken from air in order to oxidize metallic Fe, and is estimated from the TG –data measurements as w = 0.1. u is a complicate function of the other quantities and estimated from the differences between TG-data of the $NaTaO_3 + z$ Fe and $NaTaO_3 + x\,Fe_2O_{3\,u}$ composites as u = 0.2…0.6, while u=1 would yield to FeO, which was not observed in the XRD data. The sum formula yields to

$$NaTaO_3 + z\,Fe + w\,O \rightarrow NaTa_{1-x}Fe_xO_{3-y} + t\,Fe_2O_{3-u} + 2x\,e^- \quad \text{with } t = (z-x)/2 \tag{9}$$

Similarly, sintering from a certain amount m of Fe_2O_3 instead of Fe yields to the p-type composite:

$$NaTaO_3 + m\,Fe_2O_3 \rightarrow NaTa_{1-r}Fe_rO_{3-s} + v\,Fe_2O_{3-q} + s\,h^+ + (q+s)\,O \tag{10}$$
$$\text{with } r < x,\ s < y,\ q = \sim 0.5 < u$$

The *ab-initio* calculations explained in section 3, as well as the experiments, confirmed that Fe is a n-type dopant, and Ag a p-type dopant. In conventional semiconductors like Si as in $SrTiO_3$ the doping situation is straight-forward as illustrated in fig. 4 (section 2.2). Added elements from the right side in the periodic table provide one additional electron, so the material becomes n-type, those from the left side provide a hole and the material becomes p-type. In pure $NaTaO_3$ the valence of each elements are $Na^{1+}Ta^{5+}O^{2-}{}_3$. Doping with Fe, which has usual the valence Fe^{3+}, would create two holes. In contrary, as this material is a n-type material in TE-experiments, electrons are released, which cause the oxygen reduction, the same mechanism as it happens for Nb-doped $SrTiO_3$ illustrated in fig. 4 b. On the other hand, oxygen reduction of the specimens occurs, when $NaTaO_3$ is sintered with Fe_2O_3, then yielding to p-type behavior. Thus, it is concluded that the reaction path and the related oxygen partial pressure decide, whether this material is an n- or p-type material.

The thermoelectric data measured on the composite $NaTa_{1-x}Fe_xO_{3-y}$ + z Mol% Fe_2O_3 with z=32 % and produced from Fe, showed the highest n-type Seebeck voltage (-320mV at

ΔT=800K). As the exact oxygen content has not yet been measured, the reason for the Seebeck voltage remains unknown. One explanation can be found by considering percolation theory for composite materials consisting of the main phase A and inserted minor phase B. The volume fraction of 32% is the border line, where the entire connection between A-particles is changed, and connection between B-particles become dominant. In other words, around this concentration range the interfaces between A-B phase are dominant for the materials properties, while at lower concentrations A-phase and at higher concentrations the B-phase properties are dominant. This fact emphasizes that interface properties of this composite material are important.

At composite materials, the Fermi level of phase A and B are adjusted at the interface leading to a p-n-junction, when a remarkable difference between the Fermi level exists. In semiconductor engineering this is known as space charge region (SCR) which forms a large electric field on nano-scale at the p-n junction. In material science this has been emphasized also for improving properties [Gleiter et al. 2001]. In Co-based perovskite thermoelectric composite material this leads to time-dependent pyroelectric behavior [Wunderlich et al. 2009-d]. The strong electric field at the space charge region sucks the electrons towards the boundaries, in which they can travel due to the confinement of the two-dimensional electron gas (2DEG) faster than in usual ceramics. A difference in the electric field at grain boundaries between hot and cold end is necessary to explain the Seebeck voltage leading to a small net electric field macroscopically. The improvement of TE-properties due to 2DEG has been mentioned in section 2.3 especially the discovery of an ultra-high Seebeck-coefficent at the Nb-$SrTiO_3$ monolayer embedded in $SrTiO_3$ [Mune et al. 2007]. Another evidence that interfaces play an important role, is the finding that certain interfaces can filter crossing electrons according to their energy [Vashaee & Shakouri 2004]. This filtering behavior can explain enhanced thermoelectric performance, because electron-phonon interaction is changed and recombination of excited electrons is suppressed. Such consideration together with future improvement of the $NaTaO_3$ composites, such as nano-structuring or proper doping are expected to yield to materials with large Seebeck coefficient.

8. Conclusions

Historically, the intensive research and development of perovskite ceramics as microwave resonators in portable phones has accumulated much knowledge, from which Nb-$SrTiO_3$ was developed as semiconductor with high performance suitable for thermoelectric applications. The search for materials with large effective mass yielded then from Nb-$SrTiO_3$ to $NaTaO_3$. The following findings have been described in this book chapter:

(1) At present, the best *n*-type TE material is $NaTa_{1-x}Fe_xO_{3-y}$ + *t* Fe_2O_{3-u} with x = 0.14, t = 32 Mol-% and a Seebeck coefficient of 0.5 mV/K and a high closed circuit current of 0.25 mA.

(2) This material can be processed by reaction sintering of $NaTaO_3$ + *z* Fe with z =50 wt%, while sintering of $NaTaO_3$ + *r* Fe_2O_3 with r = 50 wt% leads to a *p*-type thermoelectric material.

(3) The remarkable conductivity above 500 ^oC can be improved by denser sintering (several cycles 1000oC 5h), as well as the *ZT*, in order to make $NaTaO_3$ + *z* Fe compatible with other materials.

(4) The Seebeck coefficient of the p-type-TE material $NaTa_{1-x}Ag_xO_{3-y}$ + *t* AgO_u is also 0.5 mV/K with a yet small closed circuit current of 0.001 mA.
(5) The $NaTaO_3$ + *z* Cu composite shows +/-20 mV high Seebeck voltage pulses when the heat flow is reversed, which might be utilized in a phonon flow-meter.
Further improvement of this promising material is expected. The goals for further materials development of $NaTaO_3$ – Fe_2O_3 composite are:
(1) Improvement of the sintering density,
(2) Improvement of the electric conductivity,
(3) Increase of the solubility of Fe or other elements into the cubic structure of $NaTaO_3$,
(4) Search for co-doping methods to increase of the charier concentration,
(5) Stabilization of the solubility of Ag in $NaTaO_3$ for example by co-doping of other elements
(6) Clarification of the reaction path during sintering.
(7) Finally the ultimate goal is most important: Search for n- and p-type TE-materials with higher efficiency.
This material has a great potential as thermoelectric material, especially when nano-layered composites are considered.

9. Acknowledgements

The publisher suggested this contribution as an invited paper, which is gratefully acknowledged. Experimental data were provided by Susumu Soga, Yoshiyuki Kondo, Naotoshi Okabe and Wataru Sasaki , which is appreciated gratefully.

10. References

[Baca et al. 2001] Baca L., Plewa P., Pach L., and J. Opfermann, Kinetic Analysis Crystallixation of a-Al2O3 by dynamic DTA technique, *Journal of Thermal Analysis and Calorimetry* 66 (2001) 803-813

[Bobnar et al. 2002] Bobnar V., Lunkenheimer P., Hemberger J., Loidl A., Lichtenberg F., and Mannhart J., Dielectric properties and charge transport in the (Sr,La)NbO3.5-x system, *Phys. Rev.* B 65, 155115 (2002)

[Bulusu & Walker 2008] Bulusu A., Walker D.G., Review of electronic transport models for thermoelectric materials, *Superlattices and Microstructures* 44 [1] (2008) 1-36, doi:10.1016/j.spmi.2008.02.008

[Claussen et al. 1996] Claussen N., Garcia D.E., Janssen R., Reaction Sintering of Alumina-Aluminide Alloys (3A), *J. Mater. Res.*11 [11] (1996) 2884-2888, doi: 10.1557/JMR.1996.0364

[Coey et al. 1999] Coey J.M.D., Viret M., Molnar S.von, Mixed valence magnetites, *Adv. Phys.* 48 (1999) 167

[Culp et al. 2006] Culp S.R., Poon S.J., Hickman M., Tritt T.M., Blumm H., Effect of substitutions on the thermoelectric figure of merit of half-Heusler phases at 800 °C, *Appl. Phys. Lett.* **88**, (2006) 042106 1-3, doi: 10.1063/1.2168019

[Gleiter et al. 2001] Gleiter H., Weißmüller J., Wollersheim O., Würschum R., Nanocrystalline materials: A way to solids with tunable electronic structures and properties?, *Acta materialia* 49 (2001) 737 – 745, doi:10.1016/S1359-6454(00)00221-4

[Grünberg 2001] Grünberg P, Layered magnetic structures: facts, figures, future, *J. Phys.: Condens. Matter* 13 (2001) 7691–7706, http://iopscience.iop.org/0953-8984/13/34/314

[Haeni et al.2001] Haeni, J.H., Theis C.D., Shlom, D.G., Tian W., Pan, X.Q., Chang H., Takeuchi, I., Xiang, X.D., Epitaxial growth of the first five members of the Sr_n+1 Ti_n O_3n+1 Ruddlesden–Popper homologous series, *Appl. Phys. Lett.* 78 [1] (2001) 3292-3294, doi: 10.1063/1.1371788

[Hosono et al. 2006] Hosono H., Hirano M,, Ohta H., Koumoto K. et al. "Thermoelectric conversion material based on an electron localization layer between a first and a second dielectric material" Int. Patent PCT/JP2005/020939, WO2006/054550 (2006)

[Imada M., et al. 1998] Imada, M., Fujimori, A., Tokura Y., Metal-insulator transitions, *Rev.Mod.Phys*.70[4](1998) 1039-1263, doi 10.1103/RevModPhys.70.1039

[Kato & Kudo 1998] Kato H. and Kudo A., New tantalate photocatalysts for water decomposition into H and O2, *Chem. Phys. Lett*. 295 [5–6] (1998) 487–492.

[Kennedy et al. 1999] Brendan J Kennedy B.J., Prodjosantoso A K and Howard C.J., Powder neutron diffraction study of the high temperature phase transitions in NaTaO3, *J. Phys.: Condens. Matter* 11 (1999) 6319–6327., 0953-8984/99/336319+09$30.00

[Kjarsgaard & Mitchell 2008] Kjarsgaard B.A., Mtchell R.H., Solubility of Ta in the system CaCO3 – Ca(OH)2 – NaTaO3 – NaNbO3 ± F at 0.1 GPa: implicationf for the crystallization of Pyrochlore-Group Minaerals in Carbonatites, *The Canadian Mineralogist* 46 (2008) 981-990, doi : 10.3749/canmin.46.4.981

[Kresse & Hafner 1994] Kresse, G.., Hafner, J., Ab initio molecular dynamics simulation of the liquid-metal- amorphous- semiconductor transition in germanium, *Phys. Rev. B* 4914251 (1994), doi: 10.1103/PhysRevB.49.14251

[Lee et al. 1995] Lee W.Y., Bae Y.W., Stinton D.P., Na2SO4 induced Corrosion of Si3N4 Coated by CVD with Ta2O5 *J.Am.Cer.Soc.* 78 [7] (1995) 1927-30

[Lee et al. 2006] Lee K.H., Kim S.W., Ohta H., and Koumoto K, Ruddlesden-Popper phases as thermoelectric oxides: Nb-doped SrO(SrTiO3)n (n=1,2), *J. Appl Phys* 101 (2006) 063717, doi: 10.1063/1.2349559

[Lee et al. 2007-a] Lee K.H., Muna Y., Ohta H., and Koumoto K., Thermoelectric Properties of Ruddlesden–Popper Phase n-Type Semiconducting Oxides: La-, Nd-, and Nb-Doped Sr3Ti2O7, *Int. J. Appl. Ceram. Technol.*, 4 [4] 326–331 (2007)

[Lee et al. 2007-b] Lee K.H., Kim S.W., Ohta H., and Koumoto K. *J. Appl Phys* 101 (2007) 083707, Doi: 10.1063/1.2349559

[Lee et al. 2008] Lee K.H., Muna Y., Ohta H., and Koumoto K., Thermal Stability of Giant Thermoelectric Seebeck Coefficient for SrTiO3/SrTi0:8Nb0:2O3 Superlattices at 900K, *Appl. Phys. Exp*. **1** 015007 (2008)

[Lichtenberg et al. 2001] Lichtenberg, F., Herrnberger, A., Wiedenmann, K., Mannhart, J., Synthesis of perovskite-related layered $A_nB_nO_{3n+2}$ -ABO_X type niobates and titanates and study of their structural, electric and magnetic properties, *Progress in Solid State Chemistry* 29 (2001) 1–70

[Majzlan et al.2004] Majzlan J, Navrotsky A., and Schwertmann U., Thermodynamics of iron oxides: Part III. *Geochimica et cosmochimica acta* ISSN 0016-7037 68 [5] (2004) 1049-1059, doi:10.1016/S0016-7037(03)00371-5

[Mune et al. 2007] Mune Y., Ohta H., Koumoto K., Mizoguchi T., and Ikuhara Y., Enhanced Seebeck coefficient of quantum-confined electrons in SrTiO3 /SrTi0.8Nb0.2O3 superlattices, *Appl. Phys. Lett.* **91**, 192105 (2007), doi: 10.1063/1.2809364

[Nolas et al. 2006] G.S.Nolas, Poon J., Kanatzidis M., Recent Developments in Bulk Thermoelectric Materials *MRS Bulletin* 31 (2006) 199-205; US Patent 6207888 (2001)

[Ohmoto & Hwang 2004] Ohtomo A., Hwang H. Y., A high-mobility electron gas at the LaAlO3/SrTiO3 heterointerface, *Nature* 427 [1] (2004) 423-426

[Ohsato 2001] Ohsato H., Science of tungstenbronze-type like Ba6-3xR8+2xTi18O54 (R=rare earth) microwave dielectric solid solutions, *Journal of the European Ceramic Society* 21 (2001) 2703–2711, doi:10.1016/S0955-2219(01)00349-1

[Ohta et al. 2005-a] Ohta S., Nomura T., Ohta H., and Koumoto K., High-temperature carrier transport and thermoelectric properties of heavily La- or Nb-doped SrTiO3 single crystals, *J. Appl. Phys*. 97 034106 (2005)

[Ohta et al. 2005-b] Ohta S., Nomura T., Ohta H., and Koumoto K., Large thermoelectric performance of heavily Nb-doped $SrTiO_3$ epitaxial film at high temperature, *Appl. Phys. Lett.* 87 (2005) 092108

[Ohta et al. 2007] Ohta, H., Kim, S., Mune, Y., Mizoguchi, T., Nomura, K., Ohta, S., Nomura, T., Nakanishi Y., Ikuhara Y., Hirano M, Hosono H., Koumoto, K,. Giant thermoelectric Seebeck coefficient of a two-dimensional electron gas in SrTiO3, *Nature Materials* 6 [2] (2007) 129-134, doi:10.1038/nmat1821

[Opfermann et al. 1992] Opfermann J., Kaisersberger E., An Advantageous variant of the Ozawa-Flynn-Wall analysis, *Thermochimica Acta* 203 (1992) 167-175

[Opfermann 2000] Opfermann J., Kinetic Analysis Using Multivariate Non-linear Regression. I. Basic concepts, *Journal of Thermal Analysis and Calorimetry*, 60 (2000) 641-658, doi:10.1023/A:1010167626551

[Perez-Mato et al. 2004] Perez-Mato J. M., Aroyo M., García A., Blaha P., Schwarz K., Schweifer J., Parlinski K., Competing structural instabilities in the ferroelectric Aurivillius compound SrBi2Ta2O9, *Phys. Rev. B* 70 (2004) 214111, doi: 10.1103/PhysRevB.70.214111

[Ruddlesden & Popper 1958] Ruddlesden, S.N.; Popper, P., The compound Sr3Ti2O7 and its structure, *Acta Crys.* 11 (1958) 54-55

[Ryan& Fleur 2002] Ryan M.A., Fleur J.P., Where There Is Heat, There Is a Way, *The Electrochem. Soc. Interface* (2002) 30-33 http://www.electrochem.org /publications/interface/summer2002/IF6-02-Pages30-33.pdf

[Sanders & Gallagher 2003] Sanders J. P., and Gallagher P. K., Kinetics of the oxidation of Magnetite using simultaneous TG/DSC, *Journal of Thermal Analysis and Calorimetry*, 72 (2003) 777–789, 1388 6150/2003/

[Shanker et al., 2009] Shanker V., Samal S.L., Pradhan G.K., Narayana C., Ganguli A.K., Nanocrystalline NaNbO3 and NaTaO3: Rietveld studies, Raman spectroscopy and dielectric properties, *Solid State Sciences* 11 (2009) 562–569, doi:10.1016/ j.solidstatesciences.2008.08.001

[Shirane et al. 1954] Shirane G., Newnham R., Pepinski R., Dielectric Properties and Pahse Transitions ab NaNbO3, *Phys. Rev.* 96 [1] (1954) 581- 588

[Shimizu et al. 2004] Shimizu T., Yamaguchi T., Band offset design with quantum-well gate insulating structures, *Appl. Phys. Lett.* 85 (2004)1167, doi:10.1063/1.1783012

[Sjakste et al. 2007] Sjakste J., Vast N., and Tyuterev V., Ab initio Method for Calculating Electron-Phonon Scattering Times in Semiconductors: Application to GaAs and GaP, *Phys. Rev. Lett.* 99 (2007) 236405, doi: 10.1103/PhysRevLett. 99.236405

[Sommerlate et al. 2007] Sommerlate J., Nielsch K., Boettner H., Thermoelektrische Multitalente (in German), *Physik Journal* 6 [5] (2007) 35-41 ISSN-Nr 1617-9439

[Stegk et al. 2009] Tobias A. Stegk, Henry Mgbemere, Ralf-Peter Herber, Rolf Janssen, Gerold A. Schneider, Investigation of phase boundaries in the system (KxNa1−x)1−yLiy(Nb1−zTaz)O3 using high-throughput experimentation (HTE), *Journal of the European Ceramic Society* 29 (2009) 1721–1727, doi:10.1016/ j.jeurceramsoc.2008.10.016

[Sterzel & Kuehling 2002] Sterzel, H,J, Kuehling, K, BASF, *Thermoelectric materials,* European Patent EP 1289026 A2 (2002)

[Suzuki et al. 2004] Suzuki A., Wu F., Murakami H., Imai H., High temperature characteristics of Ir–Ta coated superalloys, *Science and Technology of Advanced Materials* 5 (2004) 555–564, doi:10.1016/j.stam.2004.03.004

[Terasaki 1997] Terasaki, I. Sasago, Y., Uchinokura, K., "Large thermoelectric power in NaCo2O4 single crystals", *Phys. Rev. B*, 56 [20] (1997) R12685-R12687, doi: 10.1103/PhysRevB.56.R12685

[Vashaee & Shakouri 2004] Vashaee D. and Shakouri A., Improved Thermoelectric Power Factor in Metal-Based Superlattices, *Phys. Rev. Lett.* 92, 106103-4 (2004), doi: 10.1103/PhysRevLett.92.106103

[Vining 1991] Vining C.B., A model for the high-temperature transport properties of heavily doped n-type silicon-germanium alloys, *J. Appl. Phys.* 69 [1] (1991) 331- 341

[Wang et al. 2007-a] Y. Wang, K-H. Lee, H. Hyuga, H. Kita, K. Inaba, H. Ohta and K. Koumoto, Enhancement of Seebeck coefficient for SrO(SrTiO3)2 by Sm-substitution: Crystal symmetry restoration of disordered TiO6 octahedra, *Appl. Phys. Lett.,* 91 242102 (2007)

[Wunderlich et al. 2000] Wunderlich W., Fujimoto M., Ohsato H., Sekiguchi S., Suzuki T., Molecular Dynamics simulation about misfit dislocations at the $BaTiO_3$ / $SrTiO_3$ interface, *Thin Solid Films,* 375 [1-2] (2000) 9-14, doi:10.1016/S0040- 6090(00)01170-6

[Wunderlich et al. 2005] Wunderlich W., Ohta S., Ohta H., Koumoto K., Effective mass and thermoelectric properties of SrTiO3-based superlattices calculated by ab-initio, *Proc. Int. Conf. Thermoelectrics ICT2005*, IEEE (2005) 237-240

[Wunderlich et al. 2006-a] Wunderlich, W., Ohsato, H., Dielectric Constant-Dependence on atomic substitution of Y_2BaCuO_5 clarified by Ab-initio calculations *J. Europ. Ceram. Soc.* 16 (2006) 1869-1875 doi:10.1016/j.jeurceramsoc.2005.09.056

[Wunderlich & Koumoto 2006-b] Wunderlich W., Koumoto K., Development of high-temperature thermoelectric materials based on SrTiO3-layered perovskites, *International Journal of Materials Research* 97 [5] (2006) 657-662 http://www.ijmr.de/ directlink.asp?MK101286

[Wunderlich, 2008-a] Wunderlich W., Reduced bandgap due to phonons in SrTiO3 analyzed by ab-initio calculations, *Solid-State Electronics* 52 (2008) 1082–1087, doi:10.1016/j.sse.2008.03.017

[Wunderlich, et al. 2008-b] Wunderlich W., Ohta H., Koumoto K., Effective mass calculations of SrTiO3-based superlattices for thermoelectric applications lead to new layer design, *arXiv.org*/abs/0808.1772

[Wunderlich et al., 2009-a] Wunderlich W., Ohta H., Koumoto K., Enhanced effective mass in doped $SrTiO_3$ and related perovskites, *Physica B* 404 (2009) 2202-2212, doi:10.1016/j.physb.2009.04.012 (see also *arXiv/cond-mat* 0510013)

[Wunderlich 2009-b] Wunderlich W., $NaTaO_3$ composite ceramics - a new thermoelectric material for energy generation, *J Nucl. Mat.* 389 [1] (2009) 57-61, doi:10.1016/j.jnucmat.2009.01.007

[Wunderlich et al. 2009-c] Wunderlich W., Motoyama Y., Screening and Fabrication of Half-Heusler phases for thermoelectric applications, *Mater. Res. Soc. Symp. Proc.* Vol. 1128-U01-10 (2009)1-6., doi:10.1557/PROC-1128-U01-10, arXiv.org/abs/ 0901.1491

[Wunderlich et al. 2009-d] Wunderlich W., Fujiwara H., Difference between thermo- and pyroelectric Co- based RE-(= Nd, Y, Gd, Ce)-oxide composites measured by high-temperature gradient, http://*arxiv.org*/abs/0909.1618 (Proc. ICT 2009)

[Wunderlich & Soga 2010] Wunderlich W., Soga S., Microstructure and Seebeck voltage of Mn,Cr,Fe,Ti- added $NaTaO_3$ composite ceramics, *Journal of Ceramic Processing Research* 11 [2] 233~236 (2010)

[Xu et al. 2005] Xu J., Xue D., Yan S., Chemical synthesis of NaTaO3 powder at low-temperature, *Materials Letters* 59 (2005) 2920 – 2922, doi:10.1016/j.matlet.2005.04.043

[Yan et al., 2009] Yan S.C., Wang Z.Q., Li Z.S., Zou Z.G., Photocatalytic activities for water splitting of La-doped-NaTaO3 fabricated by microwave synthesis, *Solid State Ionics* 180 (2009) 1539–1542, doi:10.1016/j.ssi.2009.10.002

[Yamamoto et al. 2007] Yamamoto M., Ohta H., Koumoto K., Thermoelectric phase diagram in a CaTiO3–SrTiO3–BaTiO3 system, *Appl.Phys.Lett.* 90 (2007) 072101, doi: 10.1063/1.2475878

IntechOpen

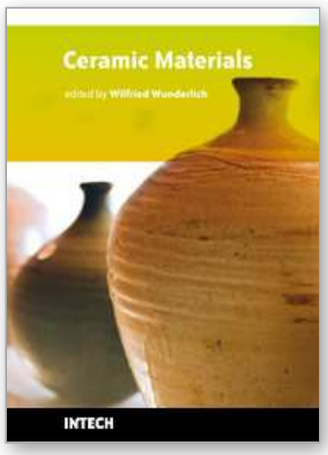

Ceramic Materials

Edited by Wilfried Wunderlich

ISBN 978-953-307-145-9

Hard cover, 228 pages

Publisher Sciyo

Published online 28, September, 2010

Published in print edition September, 2010

This is the first book of a series of forthcoming publications on this field by this publisher. The reader can enjoy both a classical printed version on demand for a small charge, as well as the online version free for download. Your citation decides about the acceptance, distribution, and impact of this piece of knowledge. Please enjoy reading and may this book help promote the progress in ceramic development for better life on earth.

How to reference

In order to correctly reference this scholarly work, feel free to copy and paste the following:

Wilfried Wunderlich and Bernd Baufeld (2010). Development of Thermoelectric Materials Based on NaTaO3 - Composite Ceramics, Ceramic Materials, Wilfried Wunderlich (Ed.), ISBN: 978-953-307-145-9, InTech, Available from: http://www.intechopen.com/books/ceramic-materials/development-of-thermoelectric-materials-based-on-natao3-composite-ceramics

INTECH
open science | open minds

InTech Europe
University Campus STeP Ri
Slavka Krautzeka 83/A
51000 Rijeka, Croatia
Phone: +385 (51) 770 447
Fax: +385 (51) 686 166
www.intechopen.com

InTech China
Unit 405, Office Block, Hotel Equatorial Shanghai
No.65, Yan An Road (West), Shanghai, 200040, China
中国上海市延安西路65号上海国际贵都大饭店办公楼405单元
Phone: +86-21-62489820
Fax: +86-21-62489821

IntechOpen